Maher, S., & Kendall, J. M. (2018). Crustal anisotropy and state of stress at Uturuncu Volcano, Bolivia, from shear-wave splitting measurements and magnitude–frequency distributions in seismicity. *Earth and Planetary Science Letters*, *495*, 38-49. https://doi.org/10.1016/j.epsl.2018.04.060

Title:

Crustal Anisotropy and State of Stress at Uturuncu Volcano, Bolivia, from Shear-Wave Splitting Measurements and Magnitude-Frequency Distributions in Seismicity

Authors:

Sean Maher[a1], J-Michael Kendall[a]

Affiliations:

a. School of Earth Sciences, University of Bristol, Wills Memorial Building, Queens Road, Bristol, UK. BS8 1RJ.

Present Address

1. Department of Earth Science, 1006 Webb Hall, University of California, Santa Barbara, CA 93106-9630

Corresponding Author:

Sean Maher

Email: smaher@umail.ucsb.edu

Tel: +1 (858)-922-5535

Keywords:

Anisotropy, Shear-wave splitting, Uturuncu Volcano, Altiplano-Puna Magma Body, stress state

Abstract

The physical signatures of unrest in large silicic magma systems are commonly observed in geophysical surveys, yet the interactions between magmatic processes and crustal stresses are often left unconstrained. Stresses in the mid and upper crust exert a strong control on the propagation and stalling of magma, and magma ascent can in turn change the magnitude and orientation of these stresses, including those associated with hydrothermal systems. This study assesses the state of stress at the restless Uturuncu Volcano in the Bolivian Andes with space, depth and time using observations of seismic anisotropy and the magnitude-frequency distributions of local earthquakes. Shear-wave splitting measurements are made for 677 events in the upper crust (1-25 km below sea level) between June 1, 2009 and March 10, 2012, and b-values are calculated using the Aki maximum likelihood method for a range of catalog subsets in the entire crust (-5 to 65 km below sea level). The b-value of the crustal events is unusually low (b=0.66±0.09), indicating that the seismogenic region features strong material with high stresses that are released with limited influence from hydrothermal fluids. The 410 good quality shear-wave splitting results have an average delay time of 0.06±0.002 s and an average percent anisotropy ranging from 0.25±0.04% to 6.2±0.94% with a mean of 1.70±0.32%. Fast shear-wave polarization directions are highly variable and appear to reflect a combination of tectonic and magmatic stresses that overprint the regional E-W compressive stress associated with the convergence of the Nazca and South American Plates. The shear-wave splitting results and b-values suggest that the upper crust beneath Uturuncu (~0-7 km below the summit) is characterized by a weak and localized hydrothermal system in a poorly developed fracture network. We conclude that stresses imposed by crustal flexure due to magmatic unrest above the Altiplano-Puna Magma Body activate crack opening on a pre-existing fault beneath the volcano, generating seismicity and a spatially variable 1-10% anisotropy above the brittle-ductile transition zone. These results suggest that strong stresses in relatively unfractured upper crustal rocks may locally inhibit fluid migration in large silicic magma systems, leading to pluton emplacement and effusive volcanism rather than explosive eruptions.

1. Introduction

Unrest in large silicic magma bodies may have significant consequences for the evolution of the continental crust and for society at large, yet our understanding of this phenomenon is limited. Intrusion and crystallization of large volumes of magma can change the density structure and chemical composition of the crust, while ascent and catastrophic eruption (VEI≈8) of such magma would undoubtedly have a global impact. Whether magma stalls or propagates to the surface is in part influenced by the stress state of the upper crust, which can both inhibit magma ascent and change in response to it (Gudmundsson, 2006). Uturuncu Volcano in the Bolivian Andes is an ideal location to study this dynamic interaction. The volcano is located in a region distinguished by large-volume explosive volcanism, and it is deforming in response to magmatic unrest above what has been called the largest magma reservoir in the Earth's continental crust (Chmielowski et al., 1999). This study investigates spatiotemporal variations in crustal stress at Uturuncu using shear-wave splitting measurements and magnitude-frequency observations of local earthquakes in a 3-year seismic dataset.

Uturuncu is an unusual stratovolcano in a region characterized by geophysical anomalies (Figure 1). Although the volcano has been dormant for 270 ka (Sparks et al., 2008; Muir et al., 2014), it has been deforming with a "sombrero uplift" morphology since satellite observations began in 1992 (Pritchard and Simons, 2002; Fialko and Pearse, 2012). This curious pattern of central uplift (1-2 cm/yr) and peripheral subsidence (~4 mm/yr) is 150 km in diameter (Henderson and Pritchard, 2013), centered ~3 km WSW of Uturuncu's summit. The source of this deformation has been modelled by various magmatic processes and geometries at depths ranging from 9 to 28 km (Fialko and Pearse, 2012 and Hickey et al., 2013, respectively).

Numerous lines of evidence suggest that the source of ground deformation is associated with magmatism at the top of the Altiplano-Puna Magma Body (APMB), a giant zone of low seismic velocity (Chmielowski et al., 1999; Zandt et al., 2003; Ward et al., 2014), low electrical resistivity (Comeau et al., 2016) and low density (Del Potro et al., 2013) at ~19-20 km depth. The APMB is the source for large eruptions that produced the calderas and ignimbrites of the 11-1 Ma Altiplano-Puna Volcanic Complex (APVC; de Silva, 1989; Salisbury et al., 2011), in which Uturuncu resides. This voluminous igneous activity is associated with the ENE subduction of the Nazca Plate beneath the South American Plate, which has thickened the crust of the Altiplano-Puna plateau to a remarkable 70 km (Figure 1; James, 1971). For a review of published models of the APMB and the source of ground deformation, the reader is referred to Table 1 of Comeau et al. (2016).

The enigmatic relationship between Uturuncu, the APVC and the APMB raises several open questions. Is the current unrest a sign of large-volume pre-eruptive magma ascent (e.g., Sparks et al., 2008), or a more benign re-organization of magmatic fluids associated with pluton emplacement (e.g., Gottsmann et al., 2017)? Why has Uturuncu had an exclusively effusive eruptive history (Muir et al., 2014) in a region otherwise distinguished by explosive volcanism? Previous studies have addressed these questions by constraining the volume (e.g., Ward et al., 2014), melt fraction (e.g., Comeau et al., 2016; Farrell et al., 2017) and chemistry (Muir et al., 2014) of the magma, but the surrounding rocks also hold important information. The stress state of the upper crust plays a crucial role in halting magma ascent (Gudmundsson, 2006) and it can record past and present perturbations by magmatic forces. This study investigates spatiotemporal variations in the stress state at Uturuncu using shear-wave splitting measurements of raypaths from events between 1 and 25 km below sea level (BSL) and seismic b-values for earthquakes in the entire crust (≤65 km BSL).

2. Background

2.1 b-values

One approach to inferring the stress state of an area is through the magnitude-frequency distributions of local earthquakes. In most cases the frequency of earthquakes decreases logarithmically with magnitude by the Gutenberg-Richter (G-R) relationship:

$$log_{10}N = a - bM, \quad (1)$$

where N is the number of earthquakes with magnitudes greater than or equal to M, and a and b are constants (Gutenberg and Richter, 1954). The b-value (b) defines the slope of the cumulative magnitude-frequency distribution such that many small earthquakes yield a high b-value and vice versa. The global average b-value for tectonic settings is close to 1.0 (Frohlich and Davis, 1993), however, *b* has been found to vary with pore fluid pressure (e.g., Wiemer and McNutt, 1997) and faulting regime (Schorlemmer et al., 2005). High b-values are commonly observed in active volcanic environments where high-temperature fluids and high pore fluid pressures lower the differential stress required to break the rock (e.g., Wilks et al., 2017). A literature review of b-values at 34 volcanoes in unrest by Roberts et al. (2015) finds that *b* varies from 1.4 to 3.5 and is never less than 1.0.

Previous studies find unusually low b-values beneath Uturuncu Volcano. Table 1 shows that published estimates of b range from 0.49±0.02 to 1.04. Using the highest number of events and the rigorous Aki maximum likelihood method, Jay et al. (2012) find a value of b=0.49±0.02. This is low not only for a volcanic environment, but for any crustal setting. It implies that the seismogenic region consists of a strong crust with a poorly developed fracture network and little to no influence on stress release by pore fluid pressure. This contradicts the prediction that *b* should be high (*b*>1.0), since sulfur-bearing fumaroles near Uturuncu's summit indicate that a hydrothermal system connects the edifice to a magmatic source of fluids (Sparks et al., 2008). Moreover, this hydrothermal system may be associated with a shallow, past or present pre-eruptive magma reservoir. This reservoir is evidenced by a zone of low shear-wave velocity (Jay et al., 2012) and low electrical resistivity (Comeau et al., 2016) at approximately -3 to 1 km BSL. These depths correspond to the pre-eruptive storage depths inferred for Uturuncu's Pleistocene lavas

(Muir et al., 2014). This study seeks to elucidate the relationship between this shallow anomaly and crustal stresses by calculating *b* with depth and time using many events and the Aki maximum likelihood method.

Table 1. Published b-values for Uturuncu Volcano.

Citation	***b***	***N***	**Study Duration (days)**	**Study Period**	M_{min}	**Method**
Sparks et al. (2008)	1.04	40	6	Apr. 1-6, 2003	unstated	linear regression
Jay et al. (2012)	0.49±0.02	1138	~365	Apr. 2009 – Apr. 2010	-0.5±0.06	maximum likelihood
Jay et al. (2012)	0.64±0.04	863	~363	Apr. 2009 – Apr. 2010 excluding Feb. 27-28, 2010	-0.37±0.09	maximum likelihood
Jay et al. (2012)	0.70	1138	~365	Apr. 2009 – Apr. 2010	-0.5	least squares regression
Jay et al. (2012)	0.78	863	~363	Apr. 2009 – Apr. 2010 excluding Feb. 27-28, 2010	-0.5	least squares regression

Alvizuri and Tape (2016)	0.90	421	~697	Apr. 12, 2010 – Mar. 9, 2012	0.0	linear regression

Note: *b* is the b-value calculated using *N* number of events by the specified method, while M_{min} is the minimum magnitude of completeness. Events on 27-28 February consist of a seismic swarm triggered by a Mw 8.8 earthquake in Maule, Chile. Note that the Alvizuri and Tape (2016) catalog is cropped to the area 22.1°S/22.6°S /67.4°W/66.9°W with depths ≤60 km.

2.2 Seismic Anisotropy and Shear-Wave Splitting

While b-values indicate the way that stress is released in the seismogenic zone, seismic anisotropy reflects the strength and orientation of the stress field itself. Anisotropy is a property of materials in which seismic velocities vary with raypath azimuth and shear-wave polarization. There are many mechanisms that lead to seismic anisotropy including the preferred orientation of crystals, and the periodic layering of materials of contrasting elastic properties. A predominant cause of anisotropy in the shallow crust is the vertical alignment of fractures and faults or aligned microcracks and pore spaces (e.g., Crampin, 1994; Baird et al., 2015). These weaknesses can open, close and change orientation on short time scales to align with the maximum horizontal compressive stress (SH_{max}).

When passing through an anisotropic fabric, shear-waves split into two quasi-orthogonal planes of particle motion (e.g., Savage, 1999). The plane that rotates towards the symmetry axis of anisotropy (i.e., the fracture plane) travels faster than its counterpart. The resulting delay time (δt) and the polarization orientation of the fast wave (ϕ) give the strength and orientation of anisotropy, respectively. The delay time is normalized by the path length to give the average percent anisotropy (*A*) along the raypath:

$$A = \frac{\delta t}{d} V_s \times 100\%, \qquad (2)$$

where d is the source-receiver distance and V_s is the shear-wave velocity of the material (e.g., Savage, 1999). This study uses a shear-wave velocity of $V_s = 3.3 \pm 0.5 \frac{km}{s}$ after the 1-D velocity model for Uturuncu by Shen et al. (2017).

Previous studies of shear-wave splitting find significant spatial variations in anisotropy around volcanoes (e.g., Baird et al., 2015), 90° temporal flips in ϕ associated with eruptions (e.g., Gerst and Savage, 2004), and systematic fluctuations of δt before and after large earthquakes (e.g., Liu et al., 1997). Consequently, spatiotemporal variations in shear-wave splitting parameters can be expected in response to magmatic pressurization such as that anticipated above the APMB.

2.3 Previous Studies of Stress and Anisotropy in the Central Andes

Previous studies of seismic anisotropy in the Central Andes identify anomalously strong anisotropy with ~NE-SW alignments in the crust of the Altiplano-Puna Plateau. Using shear-wave splitting of SKS and local S-phases, Wölbern et al. (2014) find δt of 0.3-1.2 s and ϕ sub-parallel to the NE-SW striking Uyuni-Kenayani Fault Zone and the N-S striking San Vicente Fault Zone to the northeast of Uturuncu. Using comparisons between real and synthetic receiver functions, Leidig and Zandt (2003) model two layers of anisotropy in the APVC: a surface layer of 20-30% anisotropy and a layer overlying the APMB of 15-20% anisotropy. Both layers are attributed to aligned NE-SW striking cracks that may reflect magma pathways (Leidig and Zandt, 2003). Their orientation is sub-parallel to a number of low-density “ridges” above the APMB revealed by Bouguer gravity surveys (Del Potro et al., 2013). These studies suggest a regionally oriented NE-SW SH_{max} which is oblique to the E-W orientation controlled by the convergence of the Nazca and South American Plates (Figure 1).

This study aims to improve the current understanding of the stress state in the Bolivian Altiplano by focusing on a smaller geographical area at Uturuncu. The upper crustal stress state beneath this volcano is expected to reflect an interaction between the arc-scale E-W SH_{max} controlled by plate convergence, NE-SW anisotropy revealed by previous studies, regional stresses parallel to NW-SE faults in the area, and local perturbations by magmatism associated with the APMB. We note here that sub-parallel NW-striking faults in the Central Andes have been attributed with both left-lateral strike slip and extensional displacement (Riller et al., 2001; Giambiagi et al., 2016) associated with transtension, however, the style of displacement on faults near Uturuncu is unconstrained. Complex patterns of ϕ and δt and high values of A and b are expected if magmatism and hydrothermal fluids above the APMB have perturbed the stress state.

3. Data

A large and publicly available dataset of 2659 three-component seismograms for local, regional and teleseismic earthquakes provides an ideal opportunity to study the upper crust beneath Uturuncu. The dataset was collected by ANDIVOLC network stations between April 2009 and April 2010 (Pritchard, 2009) and PLUTONS network stations between April 2010 and March 2012 (West and Christensen, 2010). The dataset spans a 3 year period and includes 48 stations in total, though not all of these were active concurrently or for the entire period; Figure 3 of Farrell et al. (2017) provides a description of PLUTONS station coverage and data dropout. Events in the available catalog range in local magnitude from -0.7 to 6.1 and have hypocenter depths of -5 to 800 km below sea level (Jay et al., 2012; Keyson and West, 2013). Most events occur in the shallow crust beneath the volcano (60% above ≤10 km BSL) with magnitudes of less than 1.0 (Figure 2). Numerous seismic swarms occur throughout the study period. The largest of these consists of 214 events on February 27th, 2010 that was triggered by an Mw 8.8 earthquake in Maule, Chile, indicating that the system is sensitive to perturbations in stress.

Of the 2659 available events, 1832 events are used for magnitude-frequency distributions and 677 are chosen for shear-wave splitting analysis. Both catalog subsets are cropped to a latitude/longitude square around the network area (21.75°S/23.00°S/66.50°W/68.00°W) to focus on seismicity in the near vicinity of Uturuncu Volcano. The magnitude-frequency distribution subset is restricted to depths in the crust (≤65 km BSL), allowing investigation of variations in *b* with time and depth in the entire crustal plumbing system beneath the volcano. The shear-wave splitting subset is limited to depths of 1-25 km BSL (~6-30 km below local relief (BLR)) to specifically target anisotropy above and below the APMB and the associated magmatic source of ground deformation.

4. Methods

4.1 b-Value calculation

All b-values are calculated empirically using the Aki maximum likelihood method,

$$b = \frac{log_{10}e}{M_{avg} - M_{min}}, \tag{3}$$

where M_{avg} is the average magnitude of the catalog and M_{min} is the minimum magnitude of completeness (Aki, 1965). M_{min} is the magnitude below which all events are not detected by the instruments, and it is determined here using the Kolmogorov-Smirnov test (Kagan, 1995) at a 20% significance level. The Kolmogorov-Smirnov test calculates the maximum difference between the Gutenberg-Richter relationship and the observed magnitude-frequency distribution with increasing discrete values of M to find an optimal probability cumulative density function and associated value of M_{min}. Values of M below M_{min} are automatically removed from the calculation (Schlaphorst et al., 2016). High and low uncertainty limits of b are calculated independently using the formulae of Shi and Bolt (1982), however, for convenience they are represented in the text as b $\pm \frac{1}{2}\left(b_{err_{high}} - b_{err_{low}}\right)$ where $b_{err_{high}}$ and $b_{err_{low}}$ are the high and low error bounds, respectively. Combining the Kolmogorov-Smirnov test with the Aki maximum-likelihood method gives a more robust estimate of b than regression methods because it tests the observed magnitude-frequency distribution against the Gutenberg-Richter relationship to find a value of M_{min} that quantitatively maximizes the fit between the two distributions.

Estimates of M_{min} are known to vary with sample size N such that smaller N leads to overestimation of M_{min} and b (e.g., Roberts et al., 2015). We therefore require a minimum sample size of 50 events. In Section 5.1 we present b-value results calculated using $N \geq 611$, well over the minimum of $N = 500$ for incomplete catalogues suggested by Roberts et al. (2015). Since our b-value results are low we conclude that they are not overestimated as a result of sample size artifacts.

4.2 Shear-wave Splitting Analysis

Shear-wave splitting is measured using a semi-automated algorithm presented in Wuestefeld et al. (2010). One window each is manually defined at the start and end of the direct shear-wave arrival, and the multi-window cluster analysis of Teanby et al. (2004) subdivides these into user-specified intervals and picks the shear-wave analysis window yielding the most stable results. A grid search is performed over all possible values of δt and ϕ to find the pair of parameters that best removes the effect of splitting. This is done by minimizing the second eigenvalue of the covariance matrix for the corrected particle motion of the quasi-transverse component of the split shear-wave (Silver and Chan, 1991). Uncertainties for δt and ϕ are calculated in the 95% confidence interval using an F test after Silver and Chan (1991).

All seismograms are treated with a two-pole bandpass Butterworth filter with corner frequencies of 2 and 12 Hz, yielding an average dominant frequency and period of 7 Hz and 0.3 s, respectively. A maximum delay time of 0.3 s is used in the shear-wave splitting analysis, however, all results with $\delta t \geq 0.15$ s are scrutinized. Windows at the start and end of the shear-wave arrival are subdivided into 10 intervals to yield 100 possible results for the cluster analysis. All seismograms are interpolated from a sample rate of 50 Hz (original) to 200 Hz to smoothen the waveforms.

Only station-event pairs with incidence angles of ≤45° from the vertical, as measured at the stations, are considered in order to eliminate spurious results with particle motion contaminated by surface-converted phases (Booth and Crampin, 1985). This incidence angle cut-off (the "shear-wave window") is relatively large compared to recommended values of 35°-40° (Savage, 1999; Booth and Crampin, 1985), however, low-velocity layers represented by the APMB and a shallower anomaly are expected to refract rays toward the vertical. Using a larger shear-wave window accounts for this effect of raypath bending and increases the number of eligible event-station pairs for shear-wave splitting analysis.

Shear-wave splitting results are visually inspected and classified into four categories: good, medium, poor and null. Good results have similar-looking fast and slow shear-waves, originally elliptical particle motion that is linearized by the correction, simple error surfaces and similar δt and ϕ results across many analysis windows (e.g., Figure 3). Poor, medium and null results feature dissimilar waveforms for fast and slow shear-wave components, particle motion that is either initially linear or initially elliptical but not linearized by the correction, complex error surfaces, and/or inconsistent δt and ϕ results across many analysis windows. Only good results are used in the interpretation of anisotropy and stress state.

5. Results

5.1 b-value Results

The b-value of events in the crust (≤65 km BSL) near the volcano is 0.66±0.09 (Figure 4a). This set of events has a minimum magnitude of completeness of 1.3, and the magnitude-frequency distribution drops below the Gutenberg-Richter relationship above $M_l \approx 3.0$. The b-value of the entire set of available events with determined magnitudes (N=2478) is 0.77±0.23

The b-value for events in the crust near the volcano is consistently low with both depth and time. b-values plotted in overlapping bins of vertical thickness with equal N indicate that b is below the global tectonic average of 1.0 at all depths in the crust (Figure 4b). b is highest near 5 km BSL (0.73±0.18), however, this apparent peak is accompanied by large uncertainty. Similarly, b-values plotted in overlapping bins of time with equal N reveal b<1.0 throughout the study period (Figure 4c). Minor fluctuations in b over time are insignificant relative to uncertainty.

It is worth noting that b was also calculated for various combinations of ranges in depth, lateral area, and time to target seismicity associated with the APMB, a shallower geophysical anomaly, and seismic swarms. These efforts yielded low b-values similar to those presented here or created unsuitably small numbers of events for use in b-value calculation (i.e., $N \leq 50$).

5.2 Shear-wave Splitting Results

The 677 events chosen for shear-wave splitting analysis contain 950 event-station pairs with incidence angles ≤45°, and 410 of these yield good-quality shear-wave splitting results. This relatively high success rate (43%) may be due to the fact that numerous seismic swarms produced nearly-identical waveforms with clear S-wave arrivals that facilitated shear-wave splitting analysis. Delay times vary from 0.01±0.00 s to 0.21±0.03 s with an average of 0.06±0.002 s, while anisotropy varies from 0.25±0.04% to 6.20±0.94% with an average of 1.70±0.32%. The most frequently recorded fast shear-wave polarization direction is NW-SE, however, ϕ values in all directions are recorded (Figure 5a). Neither fast directions nor delay times show coherent variations with time (Figure 5b, c). Fast directions show no coherent variation with event depth (Figure 5d), but high-δt outliers increase in frequency below 3 km BSL (Figure 5e). In contrast, A values decrease distinctly for events below 5 km BSL (Figure 5f).

In map view the shear-wave splitting results show significant spatial variability. Although the location of anisotropy is inherently unknown, plotting results at the midpoint of each raypath represents the fact that shear-wave splitting is accrued somewhere between the source and receiver. Figure 6 shows results plotted at the surface projection of the midpoint along a straight line connecting each hypocenter to the station from which the result was retrieved. For clarity, results are separated into two bins of 0°≤ϕ≤90° (a, c) and -90°≤ϕ≤0 (b, d). Figure 6a and b show the results for events of all depths while Figure 6c and d show only the results for events with hypocenter depths above 5 km BSL. For the shallower set of events, results with positive ϕ (i.e., ENE-WSW through NNE-SSW) cluster onto the western flank of Uturuncu (Figure 6c). In contrast, results with negative ϕ (i.e., WNW-ESE through NNW-SSE) cluster into a NW-SE elongate band extending from the western flank of Uturuncu to ~20 km to the south (Figure 6d). Near E-W ϕ can be seen to the north of Uturuncu while near N-S ϕ primarily cluster in a group of mountains to the south of the volcano.

6. Discussion

6.1 Spatial Variation in Anisotropy and b-values

The diversity of ϕ around Uturuncu reflects significant spatial variations in the orientation of anisotropy that cannot be solely explained by a subduction-controlled E-W SH_{max}. The dominant NW-SE trend of ϕ is sub-parallel to the nearby Lipez Fault Zone (Riller et al., 2001), to NW-SE elongate clusters of seismicity (Jay et al., 2012), and to the surface expression of a fault identified on the southwest flank of Uturuncu by Sparks et al. (2008). These coincidences suggest that local stresses are in part controlled by a pre-existing fault running through the volcano. This fault may have previously accommodated transtension as left-lateral strike-slip displacement associated with E-W compression and N-S gravitational spreading of the high Andes (Giambiagi et al., 2016), however, moment tensors of earthquakes beneath Uturuncu reveal positively isotropic and tensional crack opening source mechanisms (Alvizuri and Tape, 2016). The agreement of location between these moment tensors and the dominant NW-SE ϕ is interpreted as the result of outward volume expansion along a pre-existing fault caused by pressurization from magmatic inflation above the APMB. Pre-existing microcracks in the upper crust rotate to align with the SH_{max} associated with this outward volume expansion and create fault-parallel ϕ running through the volcano.

While the NW-SE population of ϕ provides evidence for a fault beneath Uturuncu, contradictory orientations in ϕ complicate this interpretation. A chaotic cluster of ϕ is observed on the west flank of Uturuncu (Figure 6a, c), which coincides with the surface expression of the center of uplift. If the uplift source is a magmatic diapir (e.g., Fialko and Pearse, 2012), pressurization of the crust due magma ascent is expected to produce a radial pattern of SH_{max} away from the center of uplift. However, contributions to the stress state by the pre-existing fault, gravitational loading by the volcano itself, and fractures formed during past episodes of ground subsidence (Perkins et al., 2016) could rotate ϕ in this region to virtually any direction. The population of ϕ on the west flank of Uturuncu of is therefore interpreted to be a direct perturbation of the stress state by pressurization associated with magma ascent.

Farther from Uturuncu, fast directions seem to reflect an interaction between the arc-scale E-W SH_{max} and stresses associated with other NW-SE and NE-SW oriented faults. North of the volcano, E-W ϕ (Figure 6) may reflect stresses imposed by the convergence of the Nazca and South American Plates and recorded by the World Stress Map 2016 (Figure 1; Heidbach et al., 2016). To the northeast of the volcano, NE-SW ϕ are sub-parallel to the

Uyuni-Kenayani Fault Zone and are in general agreement with the results of Wölbern et al. (2014). To the south of the volcano, N-S and NW-SE ϕ may reflect an extension of the fault zone beneath Uturuncu.

To extract spatial trends in ϕ and δt from the complicated set of results, shear-wave splitting measurements are stacked in grid cells of 0.12°×0.12° by the locations of surface projections of raypath midpoints (Figure 7). Stacking combines the error surfaces (e.g., Figure 3d) of two or more shear-wave splitting results to produce a single error surface, and associated ϕ and δt, which represents the best combination of the individual results. We weight shear-wave splitting results by the signal-to-noise ratio so that results with clearer S-wave arrivals are given greater weight in the stack (Restivo and Helffrich, 1999).

The stacked results (Figure 7) show that significant spatial variations in anisotropy exist even in this simplified format. Near-orthogonal ϕ in NW-SE and NE-SW orientations are found in adjacent grid cells, while N-S and E-W ϕ are also observed. The strongest patterns of ϕ are a NW-SE trend near Uturuncu and a NE-SW trend in the mountains to the northeast of the volcano. The largest delay times occur in this latter cluster while the smallest delay times occur on the NW, NE and SE flanks of Uturuncu, however, the highest values of anisotropy (A>4.0%) cluster on the flanks of the volcano (red dots in Figure 7). The discrepancy between high A and low stacked δt values reflects a disproportionate number of events with relatively shallow hypocenters (1-5 km BSL) beneath the volcano.

Analysis of the stacked shear-wave splitting results suggests that the strongest patterns of ϕ reflect the influence of pre-existing faults on the stress state at Uturuncu and the surrounding Altiplano. Furthermore, the fact that the results with the highest values of *A* cluster onto the flanks of Uturuncu suggests that anisotropy is strongest where magmatic activity interacts with these pre-existing faults.

While the shear-wave splitting measurements provide abundant information about the spatial variations in anisotropy, the b-values are less conclusive. So many of the events are concentrated beneath the volcano that the seismicity is too sparse elsewhere to calculate b-values for small areas away from the edifice. Since a large number of events is needed to calculate a meaningful b-value (e.g., Roberts et al., 2015), spatial analysis of *b* has not undertaken in this study.

6.2 Variation in Anisotropy and b-values with Depth

A distinct drop in *A* below 5 km BSL (Figure 5f) suggests that the anisotropy of the upper crust decreases below this point, however, the physical meaning of this observation is not straightforward. The location of anisotropic layers is non-unique because calculations of *A* give the average anisotropy over the entire raypath. This means that *A* is sensitive to the percent of the raypath passing through the anisotropic layer, and since raypaths used in shear-wave splitting analysis are steep, event depths can be used to constrain the depth of anisotropy. Consequently, many shear-wave splitting measurements are needed above and below a zone of anisotropy to constrain its location. The set of results presented here is used to narrow down the possible depths, thicknesses and strengths of anisotropic layer(s) beneath Uturuncu.

Figure 8 compares the observed depth distribution of average *A* with predicted distributions for four example models of anisotropy. Observed values of *A* are averaged in bins of 1 km vertical thickness by hypocenter depth. Model values of anisotropy are assigned to each vertical kilometer of material down to 25 km BSL, and a predicted distribution of *A* is found by averaging the anisotropy of each overlying kilometer. Figure 8a shows the APVC anisotropy Model B of Leidig and Zandt (2003). Figure 8b shows a new model which attributes 5% anisotropy to depths near the APMB and a shallow geophysical anomaly. Figure 8c and Figure 8d show models consisting of 1-6% anisotropy in a single layer near the surface.

Interestingly, the average observed *A* values decrease steeply from 3.05±0.61% at 1-2 km BSL to 1.71±0.31% at 5-4 km BSL, then stabilize near 1.5% below this (Figure 8). This pattern reflects the hyperbolic decay of predicted distributions of *A* beneath modelled layers of anisotropy, which obscures the boundaries between layers of material with different strengths of anisotropy. Since anisotropy in natural systems is likely to be much more complex, these models can give only a rough approximation of the location and strength of anisotropy.

Analysis of Figure 8a suggests that Model B of Leidig and Zandt (2003) clearly overestimates the strength and thickness of anisotropic layers in the APVC and yields depth distributions of A that do not agree with results presented here. The depth distribution of A for Model A of Leidig and Zandt (2003) was also considered, and it yields a very similar pattern to that of Model B. The discrepancy between the Leidig and Zandt (2003) models and the results presented here could mean that anisotropy at Uturuncu is different (i.e., weaker) from that found across the rest of the APVC, or it could reflect a measurement artifact. Leidig and Zandt (2003) use comparisons between real and synthetic receiver functions, which are sensitive to the velocity structure and to impedance contrasts throughout the crust, which are not well constrained. Since shear-wave splitting provides a more localized measure of anisotropy, and since a local change from ≥20% anisotropy to ≤10% near Uturuncu seems physically unlikely, we feel that the models presented here are more plausible.

Furthermore, Figure 8b shows that any anisotropy at the depths of the APMB and the associated ground deformation source would distort the depth profile of A away from its observed distribution. This is surprising since anisotropy is expected to be elevated near the source of magmatic pressurization above the APMB. The depth range of events for shear-wave splitting analysis used here was designed to test this hypothesis, but our results provide evidence that anisotropy is more likely located in a near-surface layer.

Figure 8b and Figure 8c show that the best fit between observed and predicted depth distributions of A occurs when 1-6% anisotropy is attributed to a layer from the surface to 0-1 km BSL. These depths lay above the range of events analyzed here (1-25 km BSL), since this study was designed to locate anisotropy close to the APMB and ground deformation source. We therefore cannot resolve the thickness, geometry and magnitude of anisotropy near the surface, but our results suggest that 1-10% anisotropy is present above 1 km BSL. This anisotropy reflects microcrack alignment in response to stresses that may promote stalling and degassing of APMB magma in the upper crust, leading to effusive eruptions or pluton emplacement. Anisotropy can be expected to increase towards the surface, where low lithostatic pressure enhances the opening of microcracks.

While the shear-wave splitting measurements show a strong decrease in *A* with depth, the b-values show no corresponding trend. The b-value is expected to increase above 1.0 near the APMB (14-15 km BSL) and near the shallower geophysical anomaly (approximately -3-1 km BSL) because magmatism and hydrothermal activity produce heightened temperatures and pore fluid pressures that reduce the differential stress required to break the rock (e.g., Wiemer and McNutt, 1997). Our results do not confirm these predictions since *b* stays below 1.0 at all depths and minor fluctuations relative to uncertainty are considered negligible.

The constant distribution of low *b* is indicative of consistently low pore fluid pressure and fracture density with depth. Since observations of fumaroles at Uturuncu's summit indicate that a hydrothermal system exists (Sparks et al., 2008), we propose that these hydrothermal fluids are highly localized within a poorly-developed fracture network. Isolation and removal of the hydrothermal fluids from the seismogenic region results in low pore fluid pressures, leading to low b-values.

More speculatively, the consistently low b-values could reflect the efficient storage of crustal stresses in competent rock such that energy is only released as relatively large-magnitude earthquakes. The stored stresses would impede magma ascent from the APMB and promote stalling and degassing in the shallow crust. This process would increase the viscosity of the melt and could ultimately make large explosive eruptions less likely by favoring shallow pluton emplacement or effusive eruptions of degassed magma. This interpretation is consistent with the lack of eruptive activity for the last 270 thousand years (Sparks et al., 2008; Muir et al., 2014).

6.3 Lack of Temporal Variation in Anisotropy and b-Values

Anisotropy and b-values were expected to change over time in response to increasing stress above the ground deformation source, however, no coherent temporal changes are observed. One explanation is that the inflation source is relatively deep, and the ground deformation is slow relative to the 3-year period of this study, so changes in stress are too subtle to observe at this temporal scale. Rapid changes in anisotropy are observed in association with eruptions (Gerst and Savage, 2004) or close to large earthquakes (Liu et al., 1997), but these did not occur at Uturuncu during the study period. Another possibility is that magma ascent (or mush reorganization) slowed during this period, as evidenced by a decrease in observed GPS uplift between 2010 and 2015 (Gottsmann et al., 2017), so the change in the stress state may have slowed as well.

It is also worth noting that the random temporal distribution of ϕ and δt is likely a consequence of the strong spatial variation in anisotropy near the volcano. The stress state is differentially controlled by different processes around the volcano, such as tectonic stress, magmatic pressurization, variations in lithology and gravitational loading by the edifice. As raypaths from events sample these different areas over time, they accrue unique shear-wave splitting parameters. These parameters seem randomly distributed when compared in a single time series but exhibit more coherent trends in space.

7. Qualitative Stress Model for Uturuncu Volcano

Figure 9 presents a qualitative interpretation of the stress state at Uturuncu in map view (a) and cross-section view (b). Away from Uturuncu and nearby faults, the stress field is parallel to the regional E-W SH_{max} controlled by the convergence of the Nazca and South American Plates. The stress field rotates to align with a NW-SE striking fault beneath Uturuncu and a NE-SW striking fault to the northeast. The near-orthogonal orientations of these faults reflects their formation during different time periods when variations in plate convergence rate, subduction angle and crustal thickness caused permutations in the stress regime of the Central Andes (Giambiagi et al., 2016). Today these faults accommodate both E-W compression associated with plate convergence and N-S extension (SH_{min}) associated with gravitational spreading of the overthickened plateau, resulting in both extensional and strike-slip displacements (Giambiagi et al., 2016).

The stress state is most complex on the west flank of Uturuncu above the magmatic inflation source. Here the pre-existing fault accommodates outward volume expansion caused by magmatic pressurization, which may be due either to magma ascent (pictured;

e.g., Fialko and Pearse, 2012) or to fluid migration within a crystal mush (Gottsmann et al., 2017). This pressurization produces a radial pattern of SH_{max} at the surface that overlaps with an adjacent radial pattern created by gravitational loading of Uturuncu's edifice (Figure 9a). Finally, remnant stresses and fossil anisotropy from past episodes of magmatic deflation and ground subsidence (Perkins et al., 2016) may preserve a pattern of concentric circles of SH_{max} around the volcano and inflation source (green rectangles, Figure 9a).

In cross-section view, the maximum principal stress axis σ_1 radiates outward from the inflation source (Gudmundsson, 2006). Ascent of melt or magmatic fluids above the APMB exerts buoyancy forces on the overlying rock that cause it to deform (e.g., Burov et al., 2003). This process pressurizes the upper crust such that the ground surface deforms. Fractures open above the brittle-ductile transition zone (BDTZ), generating seismicity with isotropic and tensional crack moment tensors (Alvizuri and Tape, 2016), and aligning to create an anisotropic fabric. The seismicity is most intense where a pre-existing fault intersects a former pre-eruptive magma reservoir made of some combination of crystallized intrusions, partial melt, hydrothermal alteration and brines (Jay et al., 2012; Comeau et al., 2016). Potential modulation of the near-surface stress state by this shallow anomaly is beyond the scope of this study but constitutes a promising direction for future research. Sulfur-bearing hydrothermal fluids are removed from the seismogenic region and transported to fumaroles at the summit (Sparks et al., 2008) by an isolated pipe, resulting in low pore fluid pressures and low b-values. The effect of pore fluid pressure on reducing effective normal stress and promoting rock failure is illustrated by the translation of the Mohr circle in Figure S1 in the supplementary material. However, the observed uniformly low b-values suggest that the effect of pore fluid pressure on rock failure beneath Uturuncu is minimal.

8. Conclusion

Interactions between crustal stresses and fractures may critically influence the behavior of fluids in active magma systems, yet the state of stress and fracture networks at restless volcanoes is often poorly constrained. We investigated the stress state at Uturuncu Volcano in the Bolivian Altiplano using the magnitude-frequency distributions of 1832 earthquakes in the crust (≤65 km BSL) and shear-wave splitting measurements of 950 raypaths from 677 events in the mid- to upper crust (1-25 km BSL). Contrary to expectations, we find no evidence for anisotropy or heightened pore fluid pressure at the depths of the Altiplano-Puna Magma Body or the associated ground deformation source. Instead, we find evidence for 1-10% anisotropy in the shallow crust (0-6 km BLR) which we attribute to the alignment of microcracks with the maximum horizontal stress above the brittle-ductile transition zone. The highest magnitude anisotropy is found in a small region near the center of the edifice. The orientation of the maximum horizontal stress is spatially variable and differentially controlled by E-W compression associated with plate convergence, N-S extension accommodated by pre-existing NE-SW and NW-SE strike-slip faults, and magma dynamics above the center of ground deformation. Unusually low b-values may reflect the shallow storage of stresses that impede magma ascent, promote pluton emplacement, and ultimately create a stress state more favorable for effusive eruptions than large explosive volcanism.

We conclude that the crust beneath Uturuncu has a weak and highly localized hydrothermal system in a poorly-developed fracture network, and that pressurization associated with magma ascent or mush re-organization above the APMB is accommodated by crustal flexure and volume expansion on a pre-existing fault under the volcano. A shallow geophysical anomaly constituting a former pre-eruptive magma reservoir likely influences the near-surface stress state, but this aspect is beyond the scope of our study. We recommend future shear-wave splitting analysis of raypaths from events above the depths studied here to further constrain the interaction between this shallow anomaly and the near-surface stress state. Ray tracing of the complete set of shear-wave splitting results would help to further constrain the location of anisotropy.

The high quality, publicly-available seismic dataset for Uturuncu provides an ideal opportunity to study and improve understanding of the influence of crustal stresses and fractures on unrest dynamics in large silicic magma systems. The results presented here suggest that strong stresses in poorly developed upper-crustal fracture networks may locally impede magma ascent from large mid-crustal reservoirs, promoting pluton emplacement and effusive volcanism.

9. References

Aki, K., 1965, Maximum likelihood estimate of b in the formula log N = a-bM and its confidence limits: Bulletin of the Earthquake Research Institute, v. 43, p. 237–239.

Alvizuri, C., and Tape, C., 2016, Full moment tensors for small events (Mw < 3) at Uturuncu volcano, Bolivia: Geophysical Journal International, v. 206, p. 1761–1783, doi: 10.1093/gji/ggw247.

Baird, A.F., Kendall, J.M., Sparks, R.S.J., and Baptie, B., 2015, Transtensional deformation of Montserrat revealed by shear wave splitting: Earth and Planetary Science Letters, v. 425, p. 179–186, doi: 10.1016/j.epsl.2015.06.006.

Booth, D.C., and Crampin, S., 1985, Shear-wave polarizations on a curved wavefront at an isotropic free surface: Geophysical Journal of the Royal Astronomical Society, v. 83, p. 31–45, doi: 10.1111/j.1365-246X.1985.tb05154.x.

Burov, E., Jaupart, C., and Guillou-Frottier, L., 2003, Ascent and emplacement of buoyant magma bodies in brittle-ductile upper crust: Journal of Geophysical Research: Solid Earth, v. 108, doi: 10.1029/2002JB001904.

Chmielowski, J., Zandt, G., and Haberland, C., 1999, The Central Andean Altiplano-Puna magma body: Geophysical Research Letters, v. 26, p. 783–786, doi: 10.1029/1999GL900078.

Comeau, M.J., Unsworth, M.J., and Cordell, D., 2016, New constraints on the magma distribution and composition beneath Volcan Uturuncu and the southern Bolivian Altiplano from magnetotelluric data: Geosphere, v. 12, p. 1391–1421, doi: 10.1130/GES01277.1.

Crampin, S., 1994, The fracture criticality of crustal rocks: Geophysical Journal International, p. 428–438.

Farrell, A.K., Mcnutt, S.R., and Thompson, G., 2017, Seismic attenuation, time delays, and raypath bending of teleseisms beneath Uturuncu volcano, Bolivia: Geosphere, v. 13, p. 699–722, doi: 10.1130/GES01354.1.

Fialko, Y., and Pearse, J., 2012, Sombrero Uplift Above the Altiplano-Puna Magma Body: Evidence of a Ballooning Mid-Crustal Diapir: Science, v. 338, p. 250–252, doi: 10.1126/science.1226358.

Frohlich, C., and Davis, S.D., 1993, Teleseismic b Values; Or, Much Ado About 1.0: Journal of Geophysical Research, v. 98, p. 631–644.

Gerst, A., and Savage, M.K., 2004, Seismic anisotropy beneath Ruapehu Volcano: A possible eruption forecasting tool: Science, v. 306, p. 1543–1547, doi: 10.1126/science.1103445.

Giambiagi, L., Alvarez, P., and Spagnotto, S., 2016, Temporal variation of the stress field during the construction of the central Andes: Constrains from the volcanic arc region (22–26°S), Western Cordillera, Chile, during the last 20 Ma: Tectonics, v. 35, p. 2014–2033, doi: 10.1002/2016TC004201.

Gottsmann, J., Blundy, J., Henderson, S., Pritchard, M.E., and Sparks, R.S.J., 2017, Thermomechanical modeling of the Altiplano-Puna deformation anomaly: Multiparameter insights into magma mush reorganization: Geosphere, v. 13, doi: 10.1130/GES01420.1.

Gudmundsson, A., 2006, How local stresses control magma-chamber ruptures, dyke injections, and eruptions in composite volcanoes: Earth-Science Reviews, v. 79, p. 1–31, doi: 10.1016/j.earscirev.2006.06.006.

Gutenberg, B., and Richter, C.F., 1954, Seismicity Of The Earth, and Associated Phenomena: Princeton University Press.

Heidbach, O., Rajabi, M., Reiter, K., and Ziegler, M., 2016, World Stress Map Database Release 2016: GFZ Data Services, doi: 10.5880/WSM.2016.001.

Henderson, S.T., and Pritchard, M.E., 2013, Decadal volcanic deformation in the central andes volcanic zone revealed by InSAR time series: Geochemistry, Geophysics, Geosystems, v. 14, p. 1358–1374, doi: 10.1002/ggge.20074.

Heuret, A., and Lallemand, S., 2005, Plate motions, slab dynamics and back-arc deformation: Physics of the Earth and Planetary Interiors, v. 149, p. 31–51.

Hickey, J., Gottsmann, J., and Del Potro, R., 2013, The large-scale surface uplift in the Altiplano-Puna region of Bolivia: A parametric study of source characteristics and crustal rheology using finite element analysis: Geochemistry, Geophysics, Geosystems, v. 14, doi: 10.1002/ggge.20057.

James, D.E., 1971, Plate tectonic model for the evolution of Central Andes: Geological Society of America Bulletin, v. 82, p. 3325–3346.

Jay, J.A., Pritchard, M.E., West, M.E., Christensen, D., Haney, M., Minaya, E., Sunagua, M., McNutt, S.R., and Zabala, M., 2012, Shallow seismicity, triggered seismicity, and ambient noise tomography at the long-dormant Uturuncu Volcano, Bolivia: Bulletin of Volcanology, v. 74, p. 817–837, doi: 10.1007/s00445-011-0568-7.

Kagan, Y., 1995, Magnitude-frequency in the European-Mediterranean distribution earthquake regions: Tectonophysics, v. 245, p. 101–105.

Keyson, L., and West, M.E., 2013, Earthquake sources near Uturuncu Volcano: presented at 2013 Fall Meeting, AGU, San Francisco, CA, December 9-13, Abstract V13b-2603,.

Leidig, M., and Zandt, G., 2003, Modeling of highly anisotropic crust and application to the Altiplano-Puna volcanic complex of the central Andes: Journal of Geophysical Research, v. 108, p. 1–15, doi: 10.1029/2001JB000649.

Liu, Y., Crampin, S., and Main, I., 1997, Shear-wave anisotropy: spatial and temporal variations in time delays at Parkfield, Central California: Geophysical Journal International, v. 130, p. 771–785, doi: 10.1111/j.1365-246X.1997.tb01872.x.

Muir, D.D., Blundy, J.D., Hutchinson, M.C., and Rust, A.C., 2014, Petrological imaging of an active pluton beneath Cerro Uturuncu, Bolivia: Contributions to Mineralogy and Petrology, v. 167, p. 1–25, doi: 10.1007/s00410-014-0980-z.

Perkins, J.P., Finnegan, N.J., Henderson, S.T., and Rittenour, T.M., 2016, Topographic constraints on magma accumulation below the actively uplifting Uturuncu and Lazufre volcanic centers in the Central Andes: Geosphere, v. 12, p. 1078–1096, doi: 10.1130/GES01278.1.

Del Potro, R., Díez, M., Blundy, J., Camacho, A.G., and Gottsmann, J., 2013, Diapiric ascent of silicic magma beneath the Bolivian Altiplano: Geophysical Research Letters, v. 40, p. 2044–2048, doi: 10.1002/grl.50493.

Pritchard, M., 2009, The life cycle of Andean volcanoes: Combining space-based and field studies: International Federation of Digital Seismograph Networks, v. Other/Seis, doi: 10.7914/SN/YS_2009.

Pritchard, M.E., and Simons, M., 2002, A satellite geodetic survey of large-scale deformation of volcanic centres in the central Andes.: Nature, v. 418, p. 167–71, doi: 10.1038/nature00872.

Restivo, A., and Helffrich, G., 1999, Teleseismic shear wave splitting measurements in noisy environments: Geophysical Journal International, v. 137, p. 821–830, doi: 10.1046/j.1365-246x.1999.00845.x.

Riller, U., Petrinovic, I., Ramelow, J., Strecker, M., and Oncken, O., 2001, Late cenozoic tectonism, collapse caldera and plateau formation in the Central Andes: Earth and Planetary Science Letters, v. 188, p. 299–311, doi: 10.1016/S0012-821X(01)00333-8.

Roberts, N.S., Bell, A.F., and Main, I.G., 2015, Are volcanic seismic b-values high, and if so when?

Journal of Volcanology and Geothermal Research, v. 308, p. 127–141, doi: 10.1016/j.jvolgeores.2015.10.021.

Salisbury, M.J., Jicha, B.R., de Silva, S.L., Singer, B.S., Jiménez, N.C., and Ort, M.H., 2011, 40Ar/39Ar chronostratigraphy of Altiplano-Puna volcanic complex ignimbrites reveals the development of a major magmatic province: Bulletin of the Geological Society of America, v. 123, p. 821–840, doi: 10.1130/B30280.1.

Savage, M.K., 1999, Seismic anisotropy and mantle deformation: what have we learned from shear wave splitting? Reviews of Geophysics, v. 37, p. 65–106, doi: 10.1029/98RG02075.

Schlaphorst, D., Kendall, J.M., Collier, J.S., Verdon, J.P., Blundy, J., Baptie, B., Latchman, J.L., Massin, F., and Bouin, M.P., 2016, Water, oceanic fracture zones and the lubrication of subducting plate boundaries-insights from seismicity: Geophysical Journal International, v. 204, p. 1405–1420, doi: 10.1093/gji/ggv509.

Schorlemmer, D., Wiemer, S., and Wyss, M., 2005, Variations in earthquake-size distribution across different stress regimes.: Nature, v. 437, p. 539–542, doi: 10.1038/nature04094.

Shen, W., Alvizuri, C., Lin, F.-C., and Tape, C., 2017, A one-dimensional seismic model for Uturuncu volcano, Bolivia, and its impact on full moment tensor inversions: Geosphere, v. 13, p. 1–10, doi: 10.1130/GES01353.1.

Shi, Y., and Bolt, B., 1982, The Standard Error of the Magnitude-Frequency b-value: Bulletin of the Seismological Society of America, v. 72, p. 1677–1687.

Siebert, L., and Simkin, T., 2002, Volcanoes of the World: an Illustrated Catalog of Holocene Volcanoes and their Eruptions: Smithsonian Institution, Global Volcanism Program Digital Information Series, http://www.volcano.si.edu/world/.

de Silva, S.L., 1989, Altiplano-Puna volcanic complex of the central Andes: Geology, v. 17, p. 1102–1106, doi: 10.1130/0091-7613(1989)017<1102.

Silver, P.G., and Chan, W.W., 1991, Shear Wave Splitting and Subcontinental Mantle Deformation: Journal of Geophysical Research, v. 96, p. 429–454, doi: 10.1029/91JB00899.

Sparks, R.S.J., Folkes, C.B., Humphreys, M.C.S., Barfod, D.N., Clavero, J., Sunagua, M.C., McNutt, S.R., and Pritchard, M.E., 2008, Uturuncu volcano, Bolivia: Volcanic unrest due to mid-crustal magma intrusion: American Journal of Science, v. 308, p. 727–769, doi: 10.2475/06.2008.01.

Teanby, N., Kendall, J.-M., and van der Baan, M., 2004, Automation of shear-wave splitting measurements using cluster analysis: Bulliten of the Seismological Society of America, v. 94, p. 453–463, doi: 10.1785/0120030123.

Ward, K.M., Zandt, G., Beck, S.L., Christensen, D.H., and McFarlin, H., 2014, Seismic imaging of the magmatic underpinnings beneath the Altiplano-Puna volcanic complex from the joint inversion of surface wave dispersion and receiver functions: Earth and Planetary Science Letters, v. 404, p. 43–53, doi: 10.1016/j.epsl.2014.07.022.

West, M., and Christensen, D., 2010, Investigating the Relationship Between Pluton Growth and Volcanism at Two Active Intrusions in the Central Andes: International Federation of Digital Seismograph Networks, v. Other/Seis, doi: 10.7914/SN/XP_2010.

Wiemer, S., and McNutt, S.R., 1997, Variations in the frequency-magnitude distribution with depth in two volcanic areas: Mount St. Helens, Washington, and Mt. Spurr, Alaska: Geophysical Research Letters, v. 24, p. 189–192, doi: 10.1029/96GL03779.

Wilks, M., Kendall, J.M., Nowacki, A., Biggs, J., Wookey, J., Birhanu, Y., Ayele, A., and Bedada, T., 2017, Seismicity associated with magmatism, faulting and hydrothermal circulation at Aluto Volcano, Main Ethiopian Rift: Journal of Volcanology and Geothermal Research, v. 340, p. 52–67, doi: 10.1016/j.jvolgeores.2017.04.003.

Wölbern, I., Löbl, U., and Rümpker, G., 2014, Crustal origin of trench-parallel shear-wave fast polarizations in the Central Andes: Earth and Planetary Science Letters, v. 392, p. 230–238, doi: 10.1016/j.epsl.2014.02.032.

Wuestefeld, A., Al-Harrasi, O., Verdon, J.P., Wookey, J., and Kendall, J.M., 2010, A strategy for automated analysis of passive microseismic data to image seismic anisotropy and fracture characteristics: Geophysical Prospecting, v. 58, p. 755–773, doi: 10.1111/j.1365-2478.2010.00891.x.

Zandt, G., Leidig, M., Chmielowski, J., Baumont, D., and Yuan, X., 2003, Seismic Detection and Characterization of the Altiplano-Puna Magma Body, Central Andes: Pure and Applied Geophysics, v. 160, p. 789–807, doi: 10.1007/PL00012557.

10. Acknowledgements

We would like to thank James Verdon for providing the MATLAB algorithm for calculating b-values and Anna Horleston for help with obtaining seismic data from IRIS. Thank you to Matt Pritchard, Michael West and their colleagues for compiling and providing the event catalog. We thank two anonymous reviewers and Stephen Sparks for their constructive feedback on an earlier draft of this paper. The map in Figure 1 was made using the SubMab 4.1 tool and all other maps were made using a Digital Elevation Model from SRTM3 data.

11. Figures

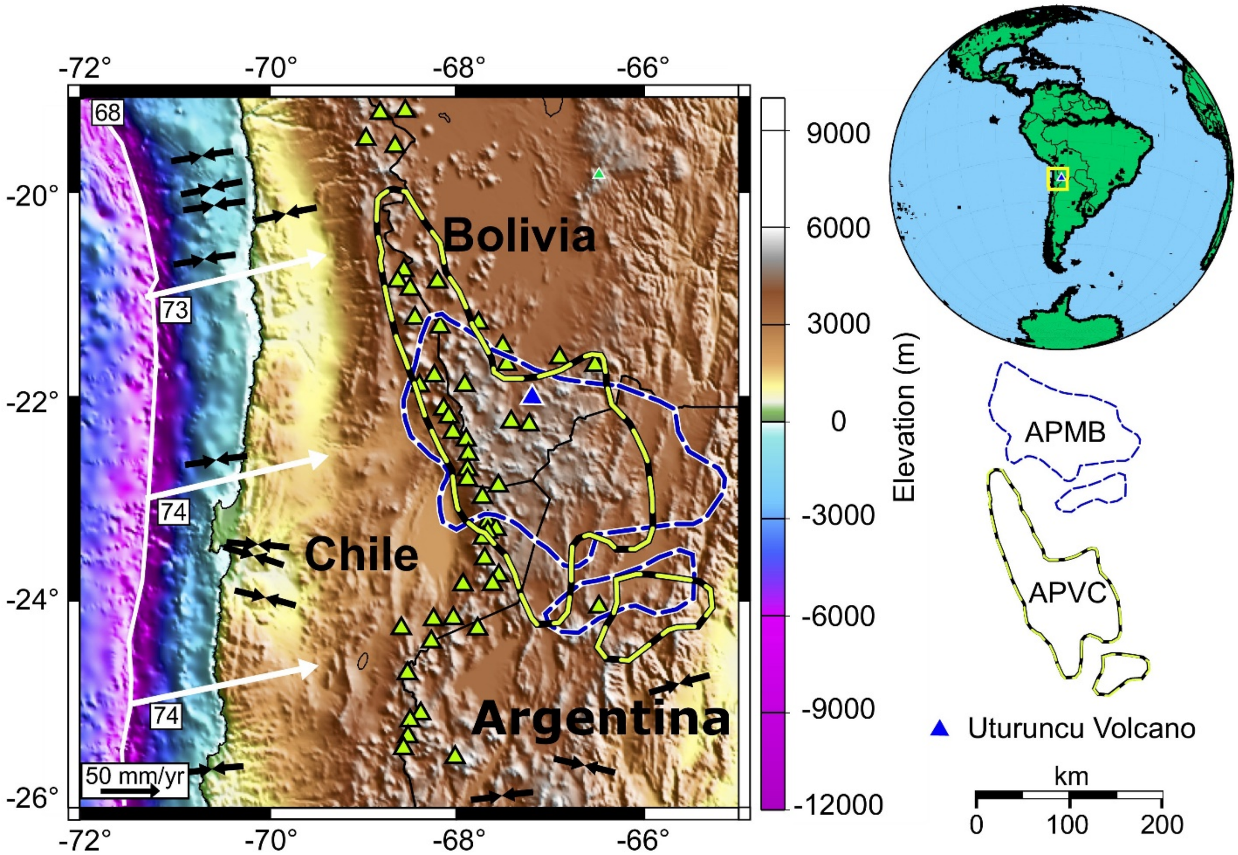

Figure 1. Tectonic and geological context of Uturuncu Volcano (blue triangle). The white line defines the boundary between the oceanic Nazca Plate and the continental South American Plate. White arrows show the subduction direction of the Nazca Plate while numbers show the rate of subduction in mm/year (Heuret and Lallemand, 2005). The eastward component of subduction is 50 mm/year. Black arrows show the orientation of maximum horizontal compressive stress from focal mechanism solutions according to the World Stress Map 2016 (Heidbach et al., 2016). Green triangles show the locations of Holocene volcanoes (Siebert and Simkin, 2002). The outlines of the Altiplano-Puna Volcanic complex and the surface trace of the Altiplano-Puna Magma Body come from de Silva (1989) and Zandt et al. (2003), respectively. The map area is shown as a yellow box on the globe.

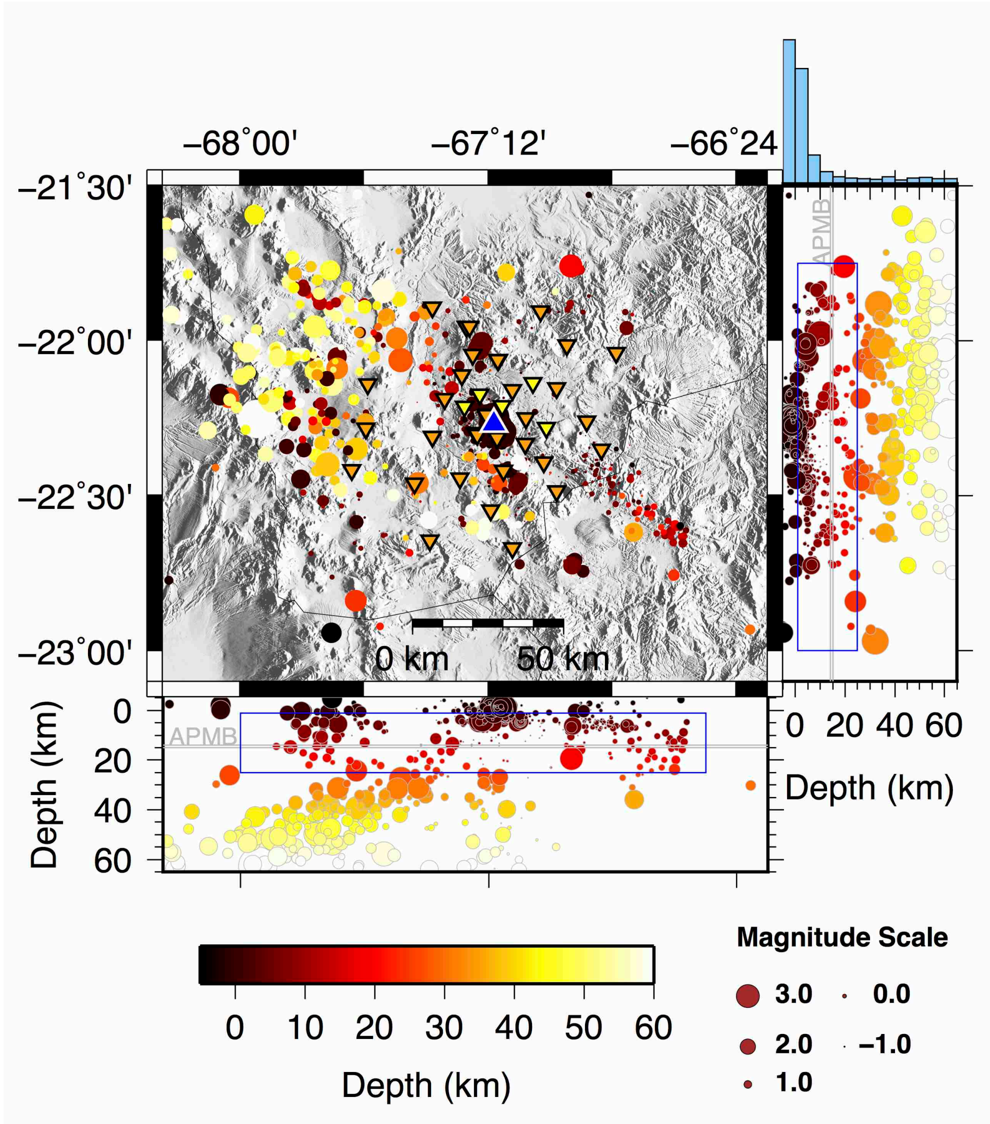

Figure 2. Distribution of crustal earthquakes in the catalog (≤65 km BSL) near Uturuncu (blue triangle). ANDIVOLC and PLUTONS stations are shown as yellow and orange inverted triangles, respectively. Plots below and right of the map show the depth distribution of events by longitude and latitude, respectively. Grey lines in these boxes show the depth and thickness of the Altiplano-Puna Magma Body (APMB) after Zandt et al. (2003). Blue boxes enclose the 677 events chosen here for shear-wave splitting analysis. Histogram at top right shows the depth distribution of events in bins of 5 km vertical thickness.

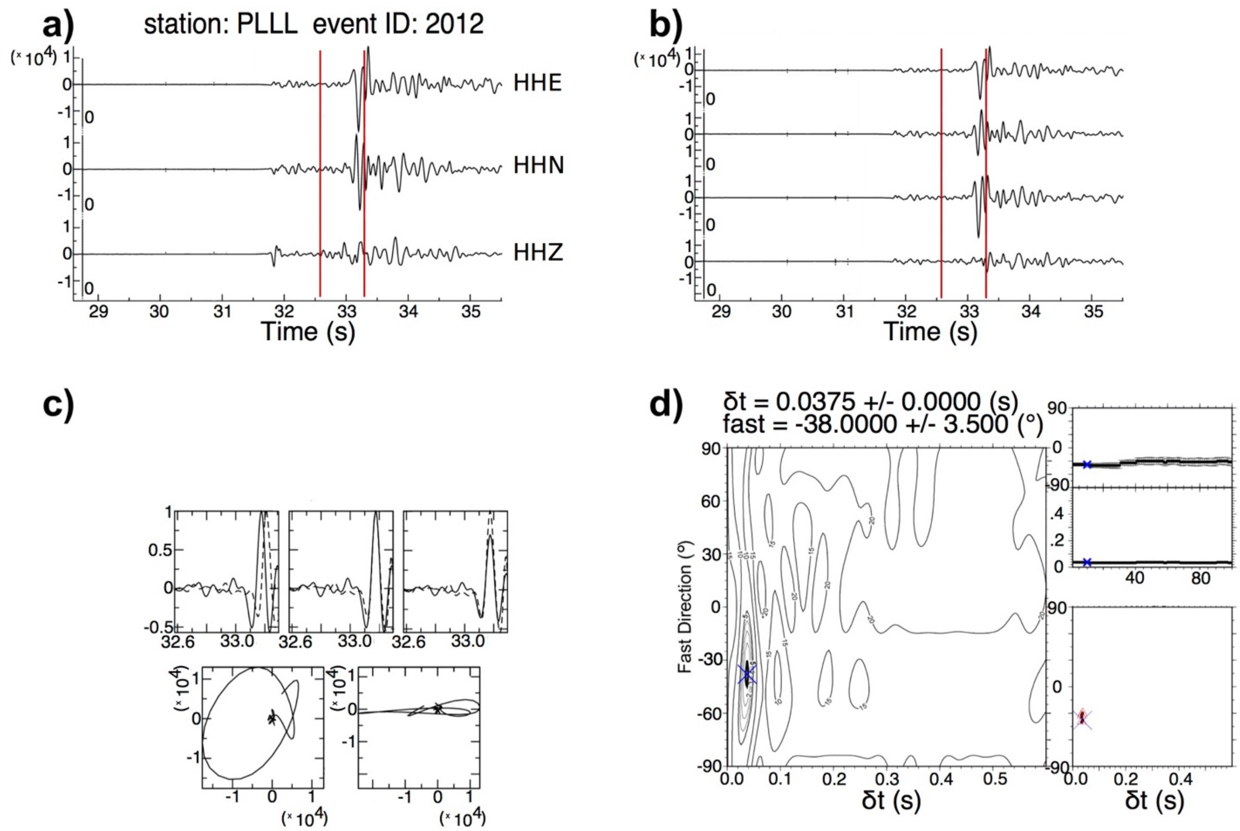

Figure 3. Example of a good quality shear-wave splitting result that illustrates the method of analysis. **a)** Three component seismograms for event 2012 (catalog ID) recorded at station PLLL (M_l=1.1, depth=4 km BSL). The start and end of the shear-wave analysis shown (red lines) are used for the final result; in practice, the algorithm considers 100 windows around the S-wave arrival. **b)** Seismograms rotated into the plane of the S-wave source polarization (top) and the plane orthogonal to it (second from top) before splitting analysis. The second from bottom and bottom seismograms, respectively, show these components after correction with the final δt and ϕ. Note that the energy has been minimized on the corrected orthogonal component. **c)** Particle motion of the fast (solid line) and slow (dashed line) S-waves before (left) and after (right) the correction. Note that the elliptical particle motion has been linearized and the energy on the corrected orthogonal component has been minimized. **d)** Error surface of the stacked results from each analysis window (left), results with uncertainties from all analysis windows (top right), and potential final results based on the error surface (bottom right). Note that the error surface is relatively simple with steep contours near the final result (cross), and the candidate results are similar with low uncertainties across many windows.

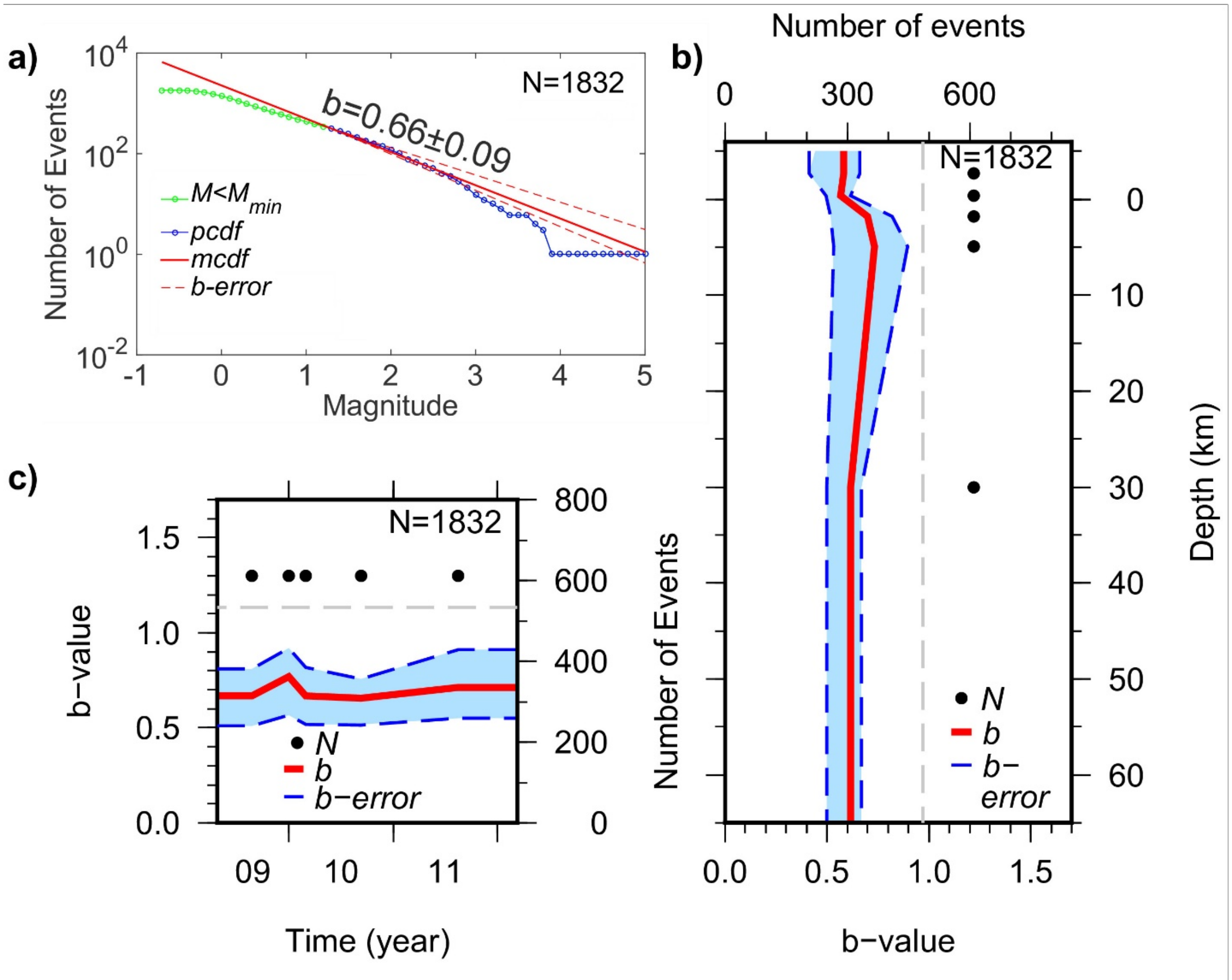

Figure 4. Results of b-value calculations using a catalog subset cropped to an area near the network area (21.75°S/23.00°S/66.50°W/68.00°W) and depths in the crust (≤65 km BSL). **a)** Cumulative magnitude-frequency distribution of the events showing a single b-value result. The K-S test has excluded magnitudes below M_{min} (green dots) and retained only magnitudes above this (blue dots; the probability cumulative density function, or pcdf) for b-value calculation. A straight line with slope *b* is fit to the pcdf (red line; the modelled cumulative density function, or mcdf) and independent high- and low-error margins are calculated for *b* (dashed red lines). **b)** b-values with depth calculated in overlapping bins of equal *N*=611 at *N*=305 spacing. The variability in vertical thickness between the bins reflects the disproportionate number of events in the upper crust. c) b-values over time calculated in overlapping bins of equal *N*=611 at *N*=305 spacing. Dashed grey lines show the global average b-value for tectonic settings (Frohlich and Davis, 1993). Black dots show the number of events per calculation and are centered in each

bin. The use of bin widths of equal N stabilizes uncertainty limits over multiple calculations compared to the use of bins of equal time or vertical thickness.

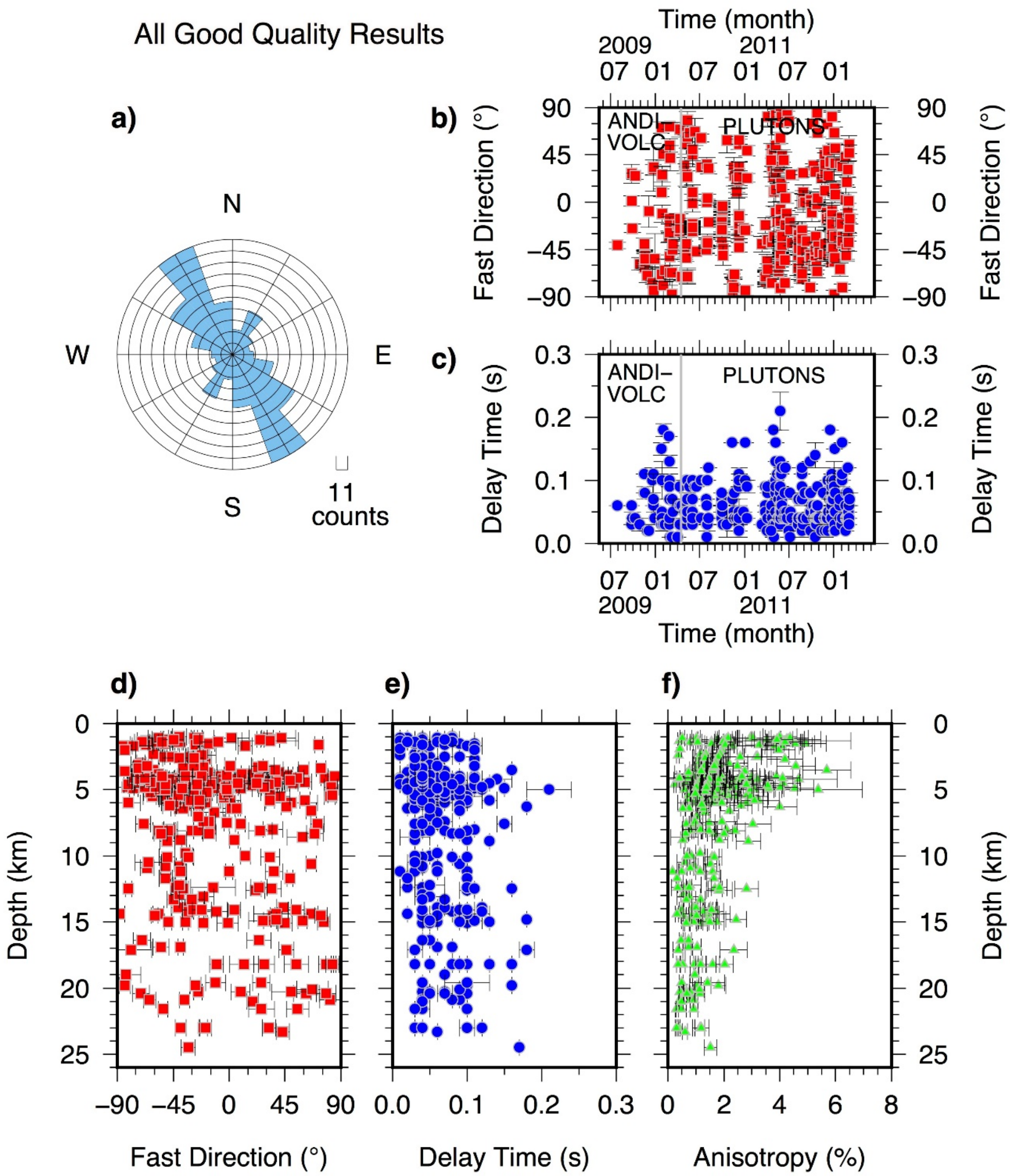

Figure 5. Variations in fast direction, delay time and percent anisotropy with time and depth for all 410 good quality splitting results. **a)** Polar histogram of all fast direction results in 20° bins **b)** Fast direction results over time. The grey line marks the transition from the ANDIVOLC network to the PLUTONS network. **c)** Delay time results over time **d)** Fast direction results with event depth below sea level **d)** Delay time results with event depth below sea level **e)** Average percent anisotropy results with event depth below sea level.

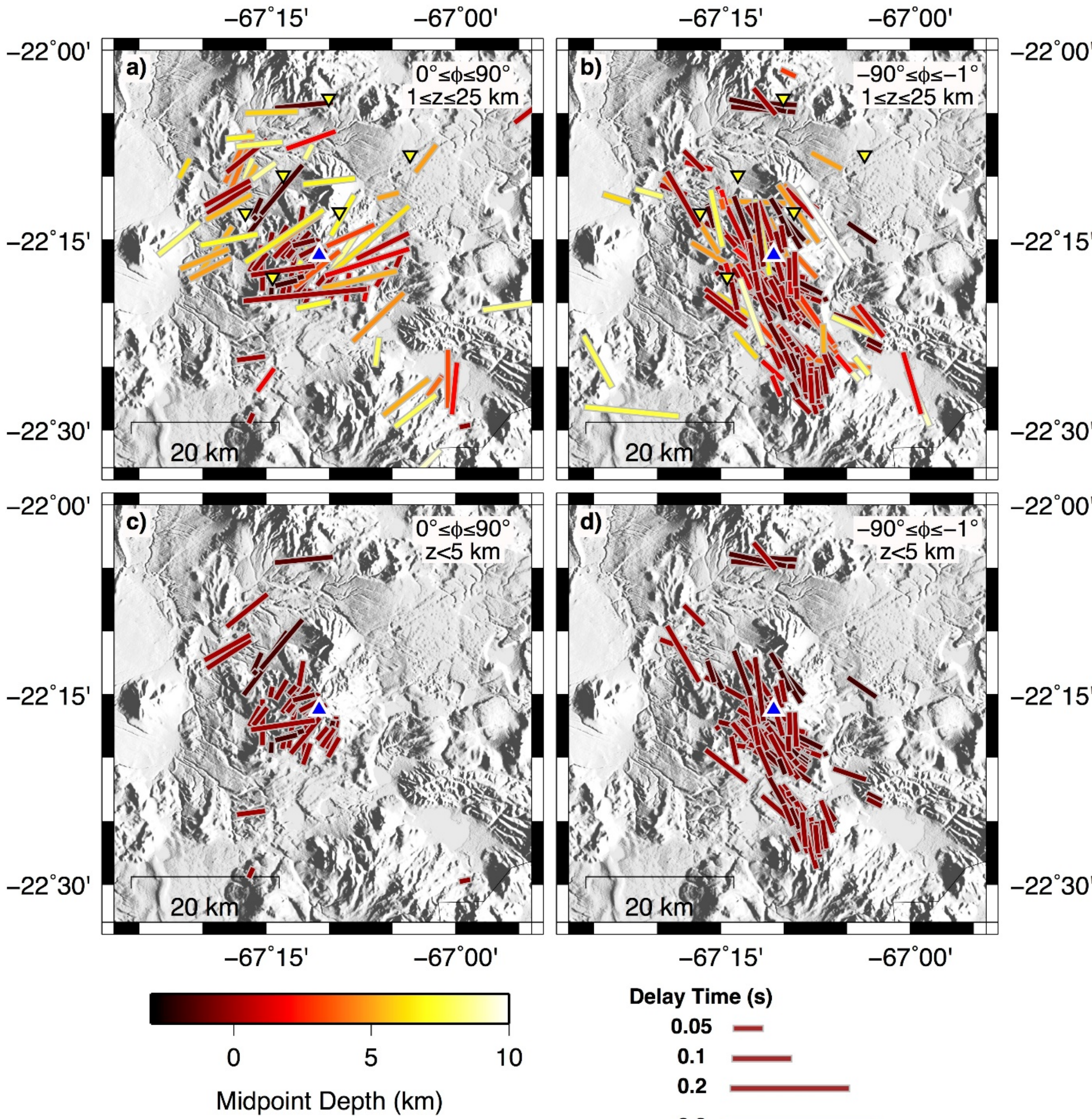

Figure 6. Map of shear-wave splitting results where measurements have been separated into two bins of ϕ and two groups of depth. Maps **a)** and **b)** show results from events of all depths binned into groups of positive ϕ (i.e., ENE-WSW to NNE-SSW) and negative ϕ (i.e., WNW-ESE to NNW-SSE), respectively. Maps **c)** and **d)** show results from events with depths less than 5 km BSL binned into groups of positive ϕ and negative ϕ, respectively. All

results are plotted at the surface projection of raypath midpoints, colored by the depth to the raypath midpoint, and scaled by δt. The blue triangle represents the summit of Uturuncu Volcano.

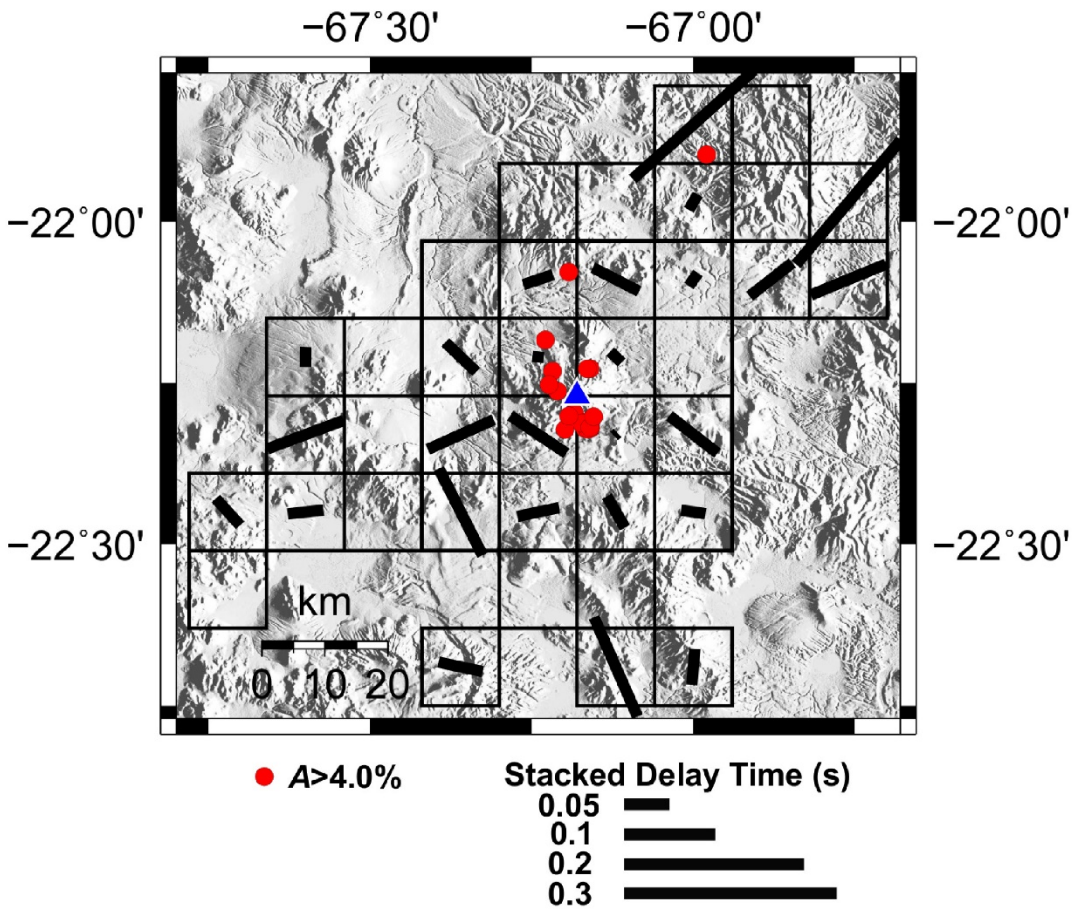

Figure 7. Map of all shear-wave splitting results stacked at the surface projection of raypath midpoints in 0.12°×0.12° cells (~13 km×13 km, pictured). Black rectangles are scaled by the stacked δt and oriented by the stacked ϕ. Red dots are plotted at the surface projection of raypath midpoint locations and show the locations of shear-wave splitting results (not stacked) with *A* values greater than 4.0%. Blue triangle: Uturuncu summit.

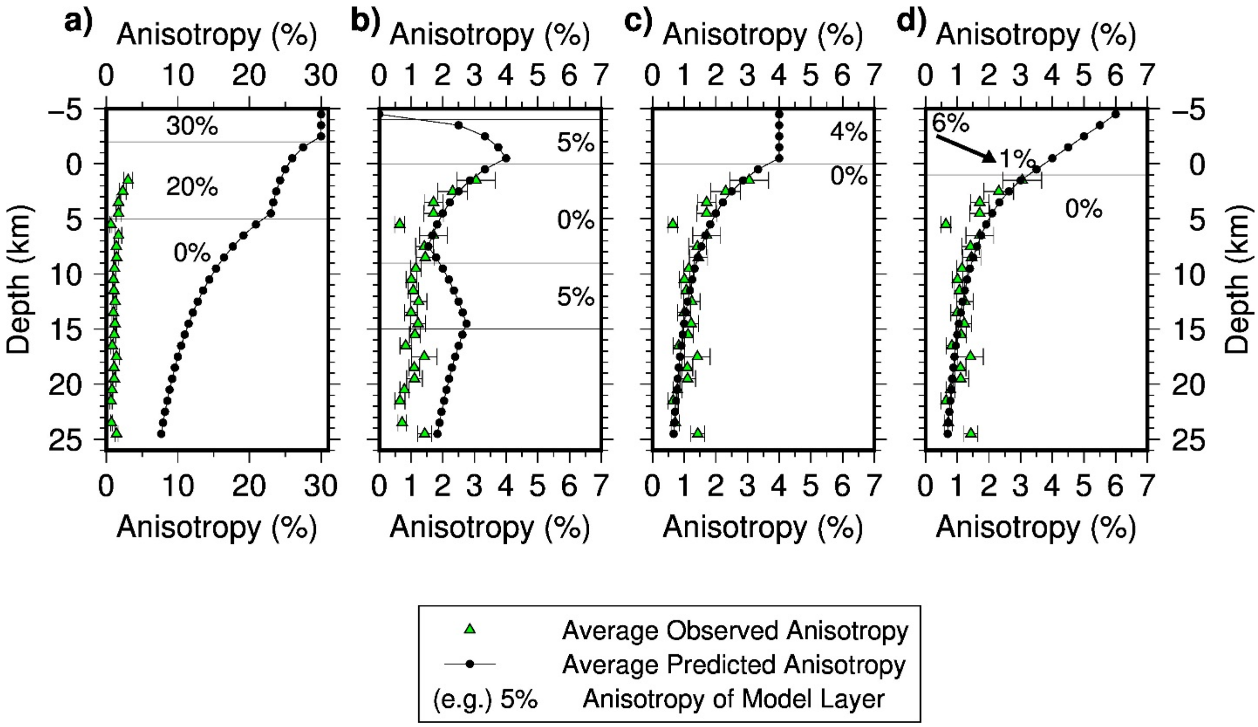

Figure 8. Comparisons between observed and modelled distributions of *A* with depth. Green triangles show the average *A* of shear-wave splitting results in this study. *A* values are averaged in bins of 1 km vertical thickness based on the hypocenter depth and the result is plotted in the center of each bin. Black dots are also centered in each bin and show the average predicted *A* for events occurring in a crust with the modelled distribution of anisotropy. The plots use the following models: **a)** Model B of Leidig and Zandt (2003) with 30% anisotropy above -2 km BSL and 20% anisotropy between -2 and 17 km BSL (note that Model A of Leidig and Zandt (2003) produces a similar distribution), **b)** two layers of 5% associated with the APMB and the near-sea-level anomaly, **c)** a near-surface layer (-5 to 0 km BSL) of 4% anisotropy, **d)** a near-surface layer (-5 to 1 km BSL) of decreasing anisotropy with depth from 6% at -5 km to 1% at 0 km. Arrow represents decreasing anisotropy with depth.

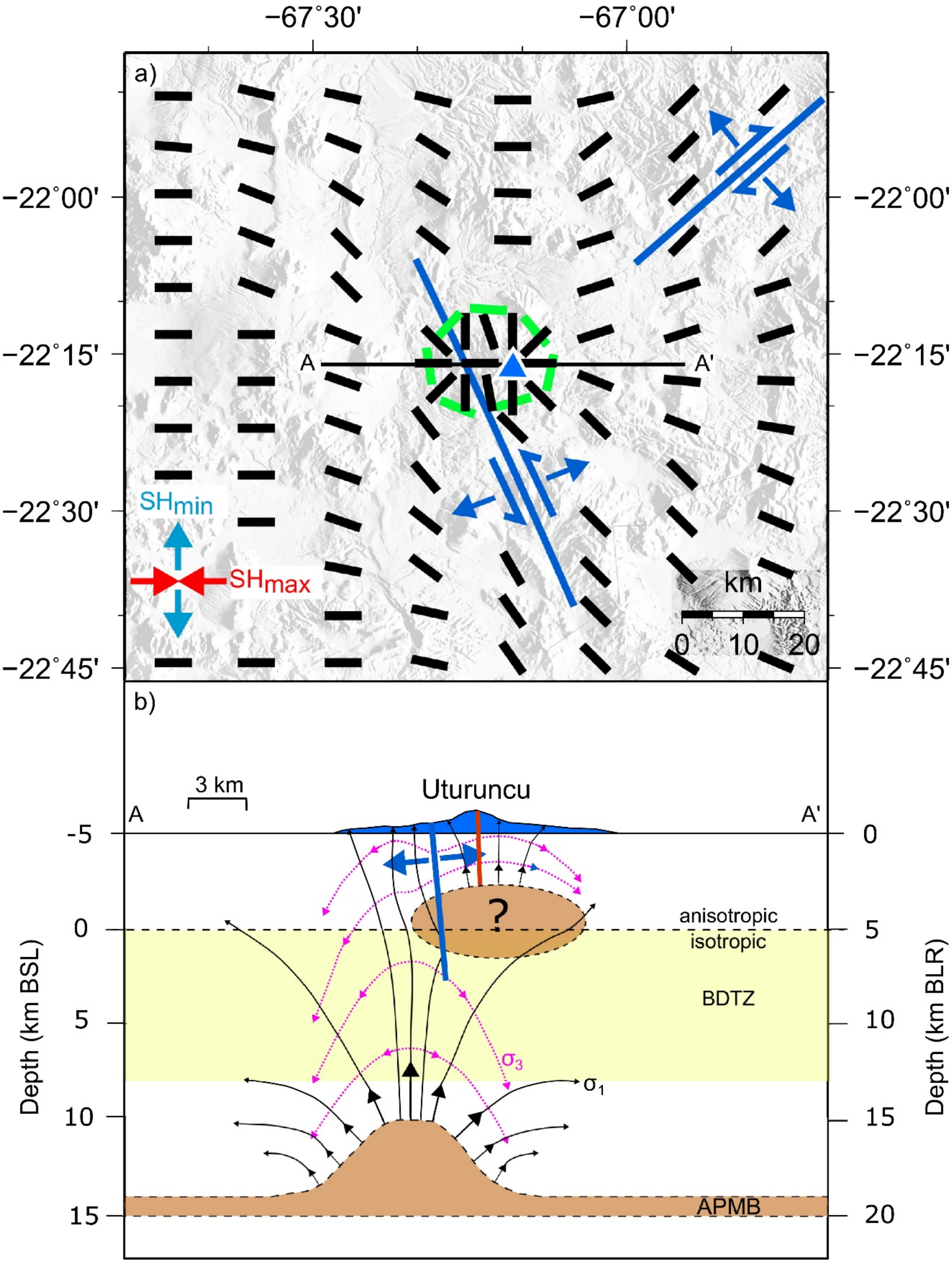
−67˚30'
−67˚00'
a)
−22˚00'
−22˚15'
−22˚30'
−22˚45'
A
A'
SHmin
SHmax
km
0
10
20
b)
3 km
Uturuncu
A
A'
-5
0
?
anisotropic
isotropic
0
5
BDTZ
5
10
σ3
σ1
10
15
APMB
15
20
Depth (km BSL)
Depth (km BLR)

Figure 9. Qualitative stress model for Uturuncu Volcano (blue triangle). The map view **a)** shows inferred orientations of contemporary SH_{max} (black rectangles) and remnant SH_{max} from past episodes of ground subsidence (green rectangles). The arc-scale E-W SH_{max} associated with plate convergence and N-S SH_{min} associated with gravitational spreading of the Andes are shown as red and blue arrows, respectively. The inferred locations and displacements of faults are shown as blue lines and blue arrows, respectively. Line A-A' shows the extent of the cross-section. **b)** Cross-sectional view of the model. The depth and thickness of the APMB and the approximate geometry of a diapiric ground deformation source are from Zandt et al. (2003) and Fialko and Pearse (2012), respectively. The shallower anomaly represents a zone of low velocity and resistivity which may constitute some combination of partial melt, crystallized intrusions and hydrothermal fluids (Jay et al., 2012; Comeau et al., 2016). Black lines show the inferred trajectories of the maximum principal stress (σ_1), while pink lines show the inferred trajectories of the minimum principal stress (σ_3) after the theoretical models of Gudmundsson (2006). The location of a fault beneath Uturuncu is inferred from the location of a fault mapped by Sparks et al. (2008), while the sense of displacement is inferred from the moment tensors of Alvizuri and Tape (2016). The boundary between anisotropic and isotropic material is inferred from the results of this study (see Fig. 8c, d) while the depth and thickness of the brittle-ductile transition zone (BDTZ; yellow area) is after Jay et al. (2012). The thin red line represents a localized pipe that transports hydrothermal fluids to fumaroles near the summit observed by Sparks et al. (2008). Note that all representations of stress direction are normalized and do not indicate the magnitude of stress.